

A high-amplitude thermal inertia anomaly of probable magnetospheric origin on Saturn's moon Mimas

C.J.A. Howett^{a,*}, J.R. Spencer^a, P. Schenk^b, R.E. Johnson^c, C. Paranicas^d, T.A. Hurford^e,
A. Verbiscer^c, M. Segura^e

^aSouthwest Research Institute, 1050 Walnut Street, Suite 300, Boulder, CO 80304, USA

^bLunar and Planetary Institute, 3600 Bay Area Blvd., Houston, TX 220758, USA

^cUniversity of Virginia, Charlottesville, VA 22904, USA

^dJohn Hopkins University, 11100 John Hopkins Road, Laurel, MD 20723, USA

^eGoddard Space Flight Center, Mail Code 693, Greenbelt, MD 20771, USA

ARTICLE INFO

Article history:

Received 7 April 2011

Revised 2 August 2011

Accepted 7 September 2011

Available online 16 September 2011

Keywords:

Satellites, Surfaces

Satellites, Composition

Magnetospheres

ABSTRACT

Spectral maps of Mimas' daytime thermal emission show a previously unobserved thermal anomaly on Mimas' surface. A sharp V-shaped boundary, centered at 0°N and 180°W, separates relatively warm daytime temperatures from a cooler anomalous region occupying low- to mid-latitudes on the leading hemisphere. Subsequent observations show the anomalous region is also warmer than its surroundings at night, indicating high thermal inertia. Thermal inertia in the anomalous region is $66 \pm 23 \text{ J m}^{-2} \text{ K}^{-1} \text{ s}^{\frac{1}{2}}$, compared to $<16 \text{ J m}^{-2} \text{ K}^{-1} \text{ s}^{\frac{1}{2}}$ outside the anomaly. Bolometric Bond albedos are similar between the two regions, in the range 0.49–0.70. The mapped portion of the thermally anomalous region coincides in shape and location to a region of high-energy electron deposition from Saturn's magnetosphere, which also has unusually high near-UV reflectance. It is therefore likely that high-energy electrons, which penetrate Mimas' surface to the centimeter depths probed by diurnal temperature variations, also alter the surface texture, dramatically increasing its thermal inertia.

© 2011 Elsevier Inc. All rights reserved.

1. Introduction

Mimas is the innermost and smallest of Saturn's mid-sized satellites, with a mean radius of 198 km. The surface of Mimas is dominantly water ice and appears bland and heavily-cratered. Cassini's Composite Infrared Spectrometer (CIRS) had two opportunities in 2010, on Cassini orbits 126 and 139 and another in 2011 on orbit 144, to observe thermal emission from Mimas' anti-Saturn hemisphere. Observations were made at a variety of local times, covering both daytime and nighttime. Further details of the observations are given in Table 1.

CIRS is a Fourier Transform Spectrometer consisting of two interferometers, which share a scan mechanism and telescope. A Michelson interferometer and two linear focal plane arrays of 10 HgCdTe detectors are used to detect mid-infrared emission. These focal planes, known as FP3 and FP4, each have a 0.273 by 0.273 mrad field of view per detector. FP3 measures from 600–1100 cm^{-1} (9.1–16.7 μm) whilst FP4 covers 1100–1400 cm^{-1} (7.1–9.1 μm). Lower wavenumbers are detected by two thermopile detectors, known as FP1, which cover 10–600 cm^{-1} (9.1–1000 μm) and have much lower spatial resolution (Flasar et al., 2004).

Mimas' surface temperatures are determined in this analysis from data taken by CIRS' FP3 detector, as it gives the best compromise between spatial resolution and sensitivity to blackbody radiation at Mimas surface temperature. The spatial resolution and achievable pointing accuracy of orbits 126 and 139 were much higher than that of orbit 144, due to the observing geometry. Thus, this analysis primarily focuses on the orbit 126 and 139 data.

2. Method and results

The pointing of all data was refined using the location of Mimas' limb in the data. As Fig. 1 shows, the limb of Mimas is visible in the orbit 126, 139 and 144 CIRS data. In orbit 126 Mimas' limb was well defined because warm daytime surface temperatures provided a clear contrast with the cold dark sky behind, and in orbit 139 the limb was also well defined because of the contrast between the cool nighttime surface temperatures on Mimas and the warm background of Saturn, as Mimas transited across it. Additional orbit 139 observations were taken that were not in Saturn transit, but were not used in this analysis because of the greater difficulty in locating surface features due to the lack of a well-defined limb. The refinement of orbit 144 pointing is more difficult since the observation is of Mimas' cooler nighttime and early morning temperatures against cold dark sky.

* Corresponding author. Fax: +1 303 546 9687.

E-mail address: howett@boulder.swri.edu (C.J.A. Howett).

Table 1

Details of the CIRS FP3 observations used in this analysis. Local time is defined as the angular rotation of the body, in degrees, since local midnight.

| Orbit | Date | Time (UT) | Sub-solar longitude (°) | Local time coverage between $\pm 20^\circ$ latitude (°) | Range (km) | Average spatial resolution (km/pixel) |
|-------|------------------|-------------|-------------------------|---|----------------|---------------------------------------|
| 126 | 13 February 2010 | 19:10–20:30 | 164–170 | 127–264 | 37,510–65,826 | 9.0 |
| 139 | 16 October 2010 | 14:27–16:53 | 85–90 | 4–130 | 73,167–101,071 | 16.0 |
| 144 | 31 January 2011 | 01:30–03:05 | 34–53 | 70–207 | 138,88–141,011 | 42.2 |

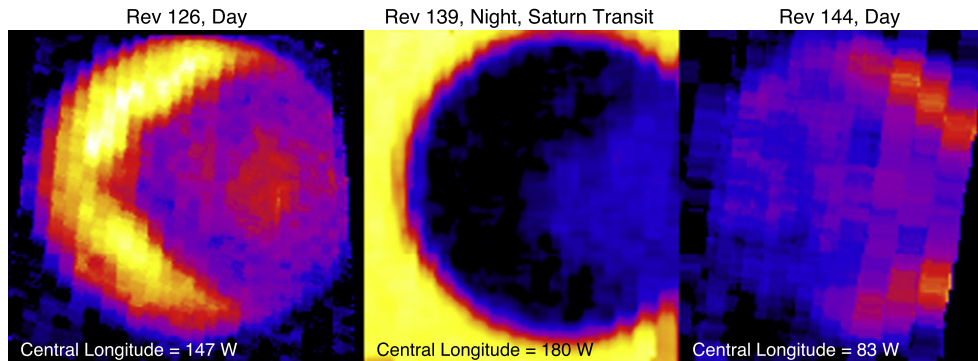


Fig. 1. 600–650 cm^{-1} CIRS FP3 day and night images of the anti-Saturn side of Mimas, taken in February 2010 (orbit 126), October 2010 (orbit 139) and January 2011 (orbit 144). The anomalously-cold region appears on the right hand side of the disk in the orbit 126 daytime image (left panel) and on the left side of the disk in the orbit 144 dayside image (right panel), which is centered at more easterly longitudes and thus shows the eastern extent of the anomaly. The same region appears anomalously warm at night (middle panel), indicating a higher thermal inertia than the rest of the disk. Saturn is in the background in the orbit 139 image.

The original pointing was determined using kernels issued by the Cassini team and NASA Planetary Science Division's Ancillary Information System (SPICE) routines (Acton, 1996). The pointing information was adjusted so that the predicted limb location coincided with the observed limb location. New longitudes and latitudes of each FP3 observation were then calculated using SPICE routines and the corrected pointing. The estimated pointing accuracy of orbit 126 and 139 data is <20 km.

The orbit 126 and 139 CIRS data were binned into $2.5^\circ \times 2.5^\circ$ bins, whilst the lower spatial resolution orbit 144 data were binned into $5.0^\circ \times 5.0^\circ$ bins. The surface temperature of each bin was determined by fitting a single blackbody curve to the mean spectrum of all the FP3 CIRS observations that fall in that bin. The resulting daytime and nighttime temperature maps are shown in Fig. 2. Both the orbit 126 and 139 maps show a V-shaped boundary, sharp at CIRS resolution, separating warmer and cooler temperatures. The apex of the V is at 0°N and 180°W , and the boundary extends in a northeasterly and southeasterly direction, approximately symmetrically about the equator. Extrapolation of the daytime data taken during orbit 144 indicates the eastern edge of the thermal anomaly is near 0° longitude. The region east of the boundary, on Mimas' leading hemisphere, is colder than its surroundings in the orbit 126 daytime observations, but is warmer than its surroundings in the orbit 139 nighttime and early morning data. This region thus displays much smaller-amplitude diurnal temperature variations than regions to the west, north, and south, which show thermal behavior more typical of other Mimas longitudes and most of the surfaces of Mimas' neighboring satellites, Tethys, Dione and Rhea (Howett et al., 2010). Thus, we refer to the region east of the boundary, on the anti-Saturn hemisphere, as the thermally-anomalous region.

Overlaid on Fig. 2 are new estimates of the energy flux of MeV electrons bombarding Mimas, updating those given in Schenk et al. (2011). Because energetic electrons in Saturn's magnetosphere drift in a retrograde direction relative to corotation they preferentially bombard Mimas' leading hemisphere. Notable improvements in the new model include the use of additional data from the Low

Energy Magnetospheric Measurement System (LEMMS) on Cassini's Magnetospheric Imaging Instrument (MIMS) (several-year averages were used) and the introduction of data from the channel E7 on LEMMS. The E7 channel is the highest energy electron channel on LEMMS and adding these data modifies the spectral slope at high energies, which turns out to be very important for the behavior of the contours particularly away from the equator. Further details on the mission averaged electron data are given in Paranicas et al. (2011).

The thermal anomaly is closely correlated spatially with an IR/UV (0.930/0.338 μm) color ratio anomaly previously observed in global maps of Mimas using Cassini Imaging Science Subsystem (ISS) data. An updated version of the global IR/UV map of Mimas, originally given in Schenk et al. (2011), is shown in Fig. 3. Though there are some inconsistencies in the latitudes and longitudes of features on the two maps, the location of the thermal and color anomalies can be compared by reference to craters near the anomaly boundaries appearing on both maps (red circles, Figs. 2 and 3). The boundaries of the thermal and color anomalies appear to be nearly identical, although the apex of the thermal anomaly appears sharper.

In the absence of endogenic emission, surface temperatures are controlled by surface bolometric Bond albedo and thermal inertia. A surface's thermal inertia describes how well it is able to store and release thermal energy, mathematically described as $\sqrt{k\rho c}$ where k is the thermal conductivity, ρ is the density and c is the specific heat. The bolometric Bond albedo is the wavelength-integrated fraction of incident solar radiation reflected in all directions by a body's surface. To investigate the cause of the anomalous temperatures seen by CIRS we determine albedo and thermal inertia for two representative regions, one outside and another inside the anomaly (shown by the boxes in Fig. 2).

The surface temperature for each of the two regions in orbits 126 and 139 was determined by fitting a single blackbody curve to the mean CIRS FP3 spectra of all the observations taken of that region (Fig. 4). Following the example of Spencer et al. (2006), the spectral noise was estimated using the difference between a

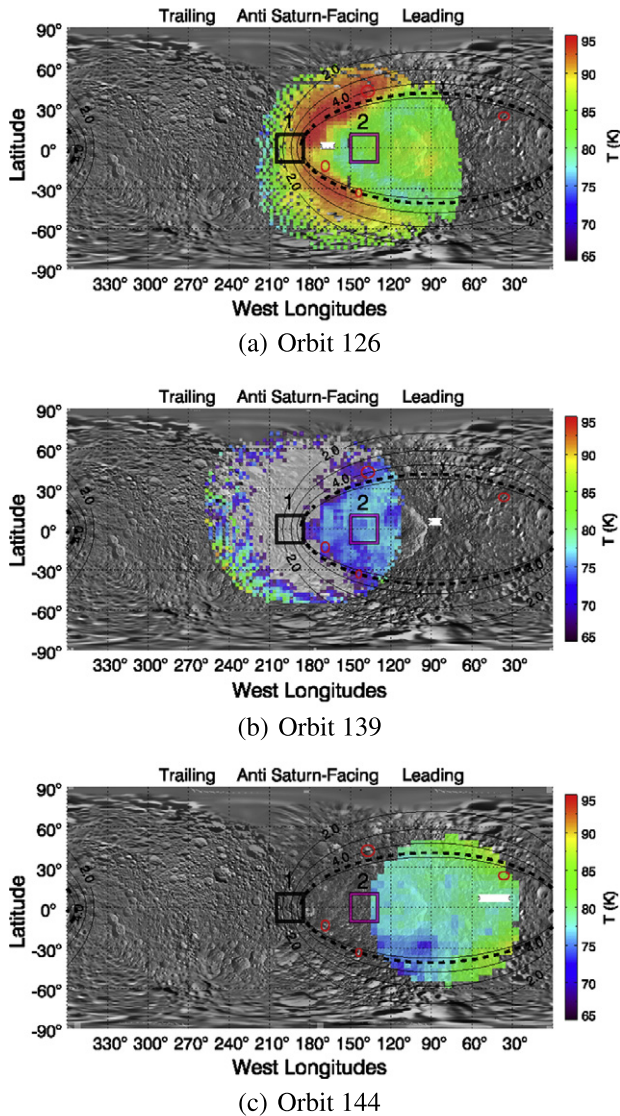


Fig. 2. Orbit 126 daytime surface temperatures (top), orbit 139 nighttime surface temperatures (middle) of Mimas and orbit 144 daytime surface temperatures (bottom). Orbit 126 and 139 data is binned into $2.5^\circ \times 2.5^\circ$ bins, whilst the orbit 144 data is binned in $5.0^\circ \times 5.0^\circ$ bins due to its lower spatial resolution. Coordinates are planetocentric and the base map is the ISS map PIA 12780. Near-limb data, with emission angle $>60^\circ$, are not shown, due to their lower spatial resolution, the difficulty in interpreting near-limb thermal emission data, which are strongly influenced by macroscopic surface roughness (Rozitis and Green, 2011), and contamination from dark sky or Saturn. The light gray shading indicates regions that have CIRS FP3 data coverage but are too cold for the temperature to be determined using FP3 data. The range of sub-solar points during the observations are indicated in both figures by white stars. The location of the two regions whose thermal surface properties are discussed in the main text are shown by the boxes labeled 1 and 2. Region 1 lies outside the anomaly and is centered at 0°N and 195°W , whilst Region 2 lies inside the anomaly and is centered at 0°N and 140°W . The red circles encompass the same craters identified in Fig. 3, to facilitate comparison of the locations of the boundaries of the thermal and IR/UV color ratio anomalies. Overlaid are contours of energetic electron power deposited into the surface per unit area ($\text{MeV cm}^{-2} \text{s}^{-1}$) determined using updated results from Cassini/MIMI. The best fitting contour to the IR/UV color ratio anomaly boundary (Fig. 3) is given by the dashed line at $5.6 \times 10^4 \text{ MeV cm}^{-2} \text{s}^{-1}$.

spectrum and its best fitting black body curve. A two-step Monte Carlo technique was then used to convert this spectral noise estimate into a temperature noise. Firstly synthetic noise with a comparable magnitude to the observed noise is created and added to the previously determined best fitting blackbody curve. In the second step the spectra (created in the first step) is fitted by a black-

body emission spectra. These two steps are repeated numerous times and the temperature error estimate is given by the standard deviation of the temperatures whose blackbody emission spectra is best able to fit the created spectra.

The approximately zero radiances of the FP3 nighttime spectra for the region outside of the anomaly show that its temperature is below the detection limit of the FP3 detector. A comparison of the mean radiance to various blackbody temperature curves indicates that the temperature in this region must be less than 65 K (Fig. 4), thus this value was used as an upper limit.

The surface thermal properties were constrained by comparing their observed nighttime temperatures (orbit 139) and daytime temperatures (orbit 126) to a 1-D diurnal surface thermal model (c.f. Spencer et al., 1989). The model used to determine Mimas' surface temperatures calculates, in one-dimension, the heat flow conducted to and away from the surface to determine the temperature as a function of depth and time of day. The upper boundary is set so that the thermal radiation and incident solar radiation are balanced with the heat conducted to and from the surface and the change in the heat content of the surface layer. The lower boundary is set to a depth at which there is negligible temperature change with the diurnal temperature cycle. The model assumes a value of unity for the emissivity and insolation variation is determined using the following model inputs: rotation rate, latitude, local time (defined as the angular rotation of the body, in degrees, since local midnight), heliocentric distance and sub-solar latitude. To determine the surface thermal properties the model requires the bolometric Bond albedo and thermal inertia to be specified. The output is a diurnal temperature curve, such as those shown in Fig. 5. The model was run for the location of each of the two regions, and the solar illumination geometry specific for each observation to determine the range of thermal inertia and albedo combinations capable of reproducing the temperatures observed at the local time of the observations (Fig. 5).

The ranges of bolometric Bond albedos capable of fitting the data outside and inside of the anomaly overlap: 0.49–0.70 and 0.56–0.62 respectively. This is consistent with the lack of a noticeable albedo boundary in visible-wavelength images. These albedos are comparable in value with those observed on Tethys, Dione and Rhea (Table 2). As expected, it is the thermal inertias that vary significantly: $<16 \text{ J m}^{-2} \text{ K}^{-1} \text{ s}^{1/2}$ outside the anomaly (these units henceforth referred to as MKS) and $66 \pm 23 \text{ MKS}$ within it. The low thermal inertias outside of the anomaly are similar to those observed on Tethys, Dione and Rhea (Howett et al., 2010), whilst those inside the anomaly are greater than but more comparable with values observed on the icy Galilean satellites (Table 2). The higher thermal inertias inside the anomalous region indicate that the surface there is less porous and/or has a higher thermal conductivity.

3. Discussion

The close spatial correlation of the thermal and IR/UV color ratio anomalies suggests a common origin. It has been proposed that high-energy (MeV) electron bombardment of Mimas' surface is responsible for the observed IR/UV color ratio variation (Schenk et al., 2011). Plasma co-rotates with the planet and thus flows around Saturn in a prograde sense, overtaking Mimas in its orbit and impacting its trailing hemisphere. However, electrons with energies above about 1 MeV flow retrograde with respect to Mimas. Their north–south motion is much faster than their longitudinal motion and these electrons therefore bombard the moon close to its leading equator. The impact patterns are represented by lens-shaped contours of energy deposition very similar in shape to the color and thermal boundary (Fig. 2). The color boundary at Mimas

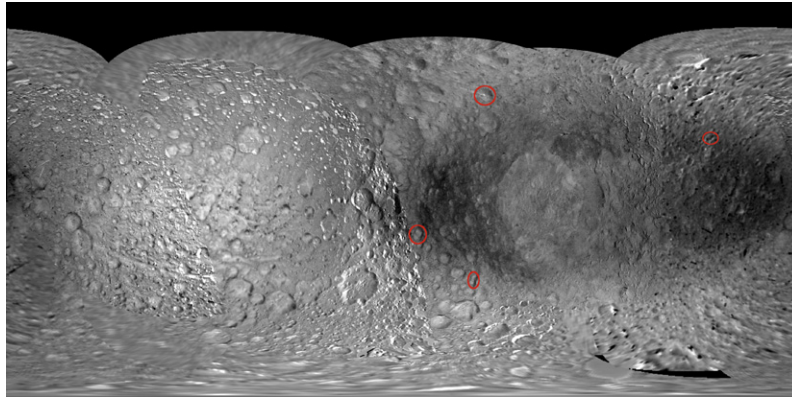


Fig. 3. IR/UV (0.930/0.338 μm) color ratio map of Mimas' surface determine from Cassini ISS data. This figure is an updated version of Fig. 3 in Schenk et al. (2011). The red circles highlight the same craters as those in Fig. 2. The longitude range is 360°W (left-hand side) to -2°W (right-hand side) and the latitude range is from 90°S (bottom) to 90°N (top).

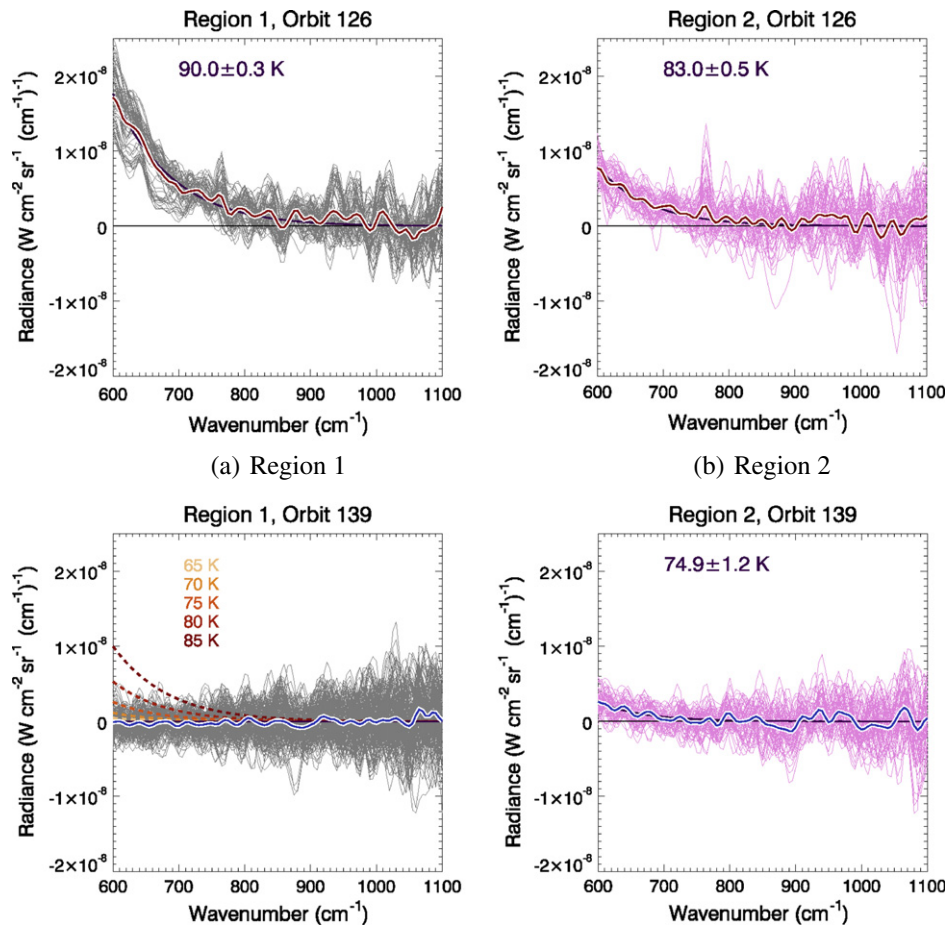


Fig. 4. CIRS FP3 spectra for both regions for orbits 126 and 139. The mean spectra are shown in red for orbit 126 and blue for orbit 139, in addition to the individual spectra in gray and pink respectively. Both the value of the best fitting blackbody temperature curve to the mean spectra and the curve itself are shown in each subfigure in purple. For Region 1, orbit 139 (bottom left), where no surface thermal emission was detected, blackbody temperature curves for a number of temperatures between 65 and 85 K are compared to the observed spectrum to determine an upper limit to the surface temperature.

corresponds to an electron energy deposition rate contour of about $5.6 \times 10^4 \text{ MeV cm}^{-2} \text{ s}^{-1}$ (Schenk et al., 2011). The contour corresponding to the boundary of the thermal anomaly is harder to determine due to its poorer spatial correlation, however it appears to be similar to that of the color anomaly.

Electrons (1–10 MeV) are expected to penetrate 0.5–5 cm into Mimas' water ice surface (Zombeck, 1982; Cooper et al., 2009),

exciting water molecules along their path though the ice. Diurnal temperatures probe thermophysical properties over a depth range given by the thermal skin depth δ , the penetration depth of the diurnal wave, it is defined as $l/\rho c \sqrt{\omega}$ where l is thermal inertia, ρ is the surface density, c is the specific heat and ω is the angular velocity of rotation. Assuming the specific heat of water ice at 90 K, $0.8 \text{ J K}^{-1} \text{ g}^{-1}$, and the density of non-porous ice at 93 K,

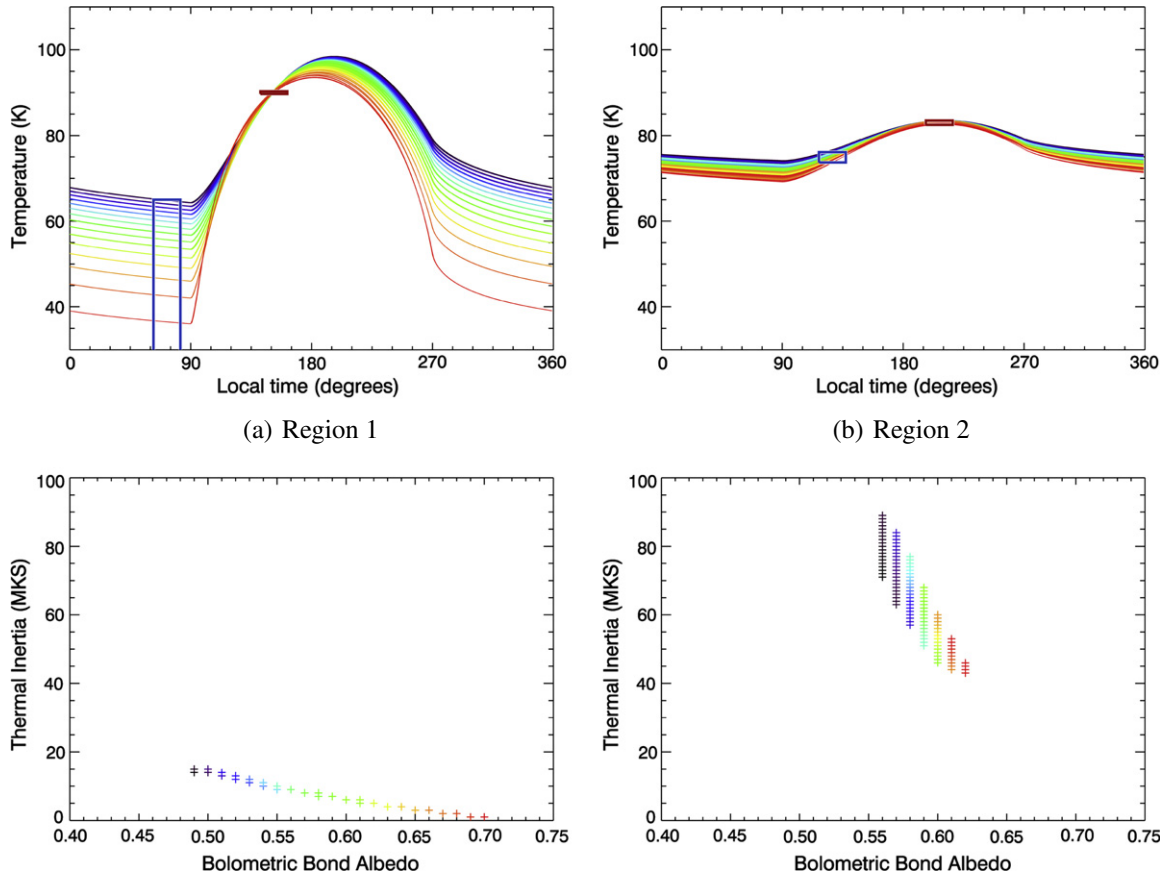


Fig. 5. Top – Diurnal curves that are able to fit both the observed orbit 126 daytime (red boxes) and orbit 139 nighttime/dawn (blue boxes) temperatures for Region 1 (left) and Region 2 (right), which lie outside and inside the anomaly respectively. The nighttime temperatures for Region 1 are below the sensitivity of the FP3 detector and therefore only an upper limit constraint is used. Bottom – The colored crosses indicate the bolometric Bond albedo and thermal inertia combinations that produce the diurnal curves that are shown in corresponding colors in the top figures. Regions 1 and 2 are shown on the left and right respectively. Albedos between 0.20 and 0.80 were sampled in increments of 0.01 and thermal inertias between 1 and 100 MKS were sampled in increments of 1 MKS.

Table 2

Thermal inertia and bolometric Bond albedo values inside and outside of Mimas' thermal anomaly are compared to values in the literature for both jovian and saturnian icy satellites.

| Target | Bolometric Bond albedo | Thermal inertia (MKS) | Skin depth ^a (cm) | Reference |
|--------------------------------|------------------------|-----------------------|------------------------------|--|
| <i>Mimas – this work</i> | | | | |
| Outside the anomaly (Region 1) | 0.60 ± 0.11 | <16 | <0.49 | |
| Inside the anomaly (Region 2) | 0.59 ± 0.03 | 66 ± 23 | 1.31–2.71 | |
| <i>Jovian satellites</i> | | | | |
| Io | 0.52 | 70 | 0.06 | Simonelli et al. (2001) Rathbun et al. (2010) |
| Europa | 0.55 | 70 | 4.14 | Spencer (1987) |
| Ganymede | 0.32 ± 0.04 | 70 ± 20 | 5.88 | Spencer (1987) |
| Callisto | 0.20 ± 0.04 | 50 ± 10 | 6.41 | Spencer (1987) |
| <i>Saturnian satellites</i> | | | | |
| Mimas | $0.49^{+0.05}_{-0.14}$ | 19^{+57}_{-9} | 0.58 | Howett et al. (2010) |
| Tethys | 0.67 ± 0.11 | 9^{+10}_{-9} | 0.39 | Howett et al. (2010) |
| Dione | 0.63 ± 0.15 | 11^{+18}_{-4} | 0.57 | Howett et al. (2010) |
| Rhea (trailing) | $0.57^{+0.20}_{-0.26}$ | 8^{+12}_{-5} | 0.53 | Howett et al. (2010) |
| Rhea (leading) | $0.63^{+0.11}_{-0.12}$ | 9^{+9}_{-5} | 0.60 | Howett et al. (2010) |
| Iapetus (trailing) | $0.31^{+0.15}_{-0.17}$ | 20^{+13}_{-8} | 5.59 | Howett et al. (2010) |
| Iapetus (leading) | 0.10^b | 14^{+7}_{-8} | 3.91 | Howett et al. (2010) |

^a The skin depth is calculated using each target's own rotation rate and a porosity of 0.5, a surface density of 0.934 g cm^{-3} and the specific heat for water ice at 90 K, $0.8 \text{ J K}^{-1} \text{ g}^{-1}$ (Spencer and Moore, 1992), the exception is for Io where the same porosity is assumed but a specific heat and density of basalt flows is assumed, $15 \text{ J K}^{-1} \text{ g}^{-1}$ and 2.6 g cm^{-3} respectively (Davies, 1996).

^b Indicates this value is an upper limit.

0.934 g cm^{-3} , for Mimas' rotation rate of 0.942 Earth days $\delta = 0.0152l/(1 - p) \text{ cm}$ where p is porosity and thermal inertia is

in MKS. For $I = 16 \text{ MKS}$, the upper limit of the thermal inertia outside of the anomalous region $\delta = 0.24/(1 - p) \text{ cm}$, whilst for a

thermal inertia of 66 MKS representative of values inside the anomaly, $\delta = 1.0/(1 - p)$ cm. Thus, assuming the porosity of both regions is comparable and of the order of tens of percent the skin depth outside of the anomalous region will be lower than inside of it (<0.49 cm compared with 1.31–2.71 cm). This is comparable to the mean range of few MeV electrons, so it is plausible that electron bombardment could affect ice properties to sufficient depth to produce the observed effect on surface temperatures.

The effect on an icy surface's thermal inertia and UV/IR color ratio of high-energy electron bombardment is not understood in detail, but increases in thermal inertia are a plausible consequence of the irradiation. It has been shown that the surface of a vapor deposited ice layer compacts when bombarded by high energy (100 keV) ions (Baragiola et al., 2008). This has been suggested to occur by the preferential destruction of small pores in the ice or due to small pores coalescing into larger ones. The very low thermal inertias of the regoliths of Saturn's icy satellites (Howett et al., 2010) may result from a particulate surface with very limited contact area between grains, resulting in very low thermal conductivity. The conduction between grains could thus be increased if molecules mobilized by electron bombardment increased the contact area between grains (essentially gluing grains together), a process often referred to as sintering. Enhanced adhesion between materials has been seen in laboratory studies (e.g. Ingemarsson et al., 1989; Raut et al., 2008). This same radiation also may produce defects locally in the ice that can increase UV scattering and thus increase the UV/IR color ratio.

Other processes, including ion bombardment, impact gardening, and deposition of E-ring material, must also be altering Mimas' surface. However, the fact that color and thermal inertia variations are dominated by a pattern that matches the expected high-energy electron flux indicates that those other processes are either less important or much more spatially uniform. The remarkably sharp thermal inertia boundary might result from the balance between increasing thermal inertia due to electron impact and decreasing thermal inertia due to a competing process such as impact gardening, if each process proceeds to saturation in the regions where it dominates.

If the thermal and/or IR/UV color ratio anomalies observed on Mimas are caused by high-energy electron bombardment of the surface then a similar thermal anomaly is expected on Tethys, where a similar IR/UV color anomaly is observed (Schenk et al., 2011). Active resurfacing of Enceladus is likely to mask any magnetospherically-generated thermal anomaly there, and no equivalent color anomaly is seen on Enceladus (Schenk et al., 2011). Similar anomalies might be expected at the icy Galilean satellites, which experience an even higher flux of energetic electrons (Paranicas et al., 2001; Jun et al., 2005), and puzzling latitude-dependent nighttime thermal inertia anomalies are seen on Europa's leading side (Rathbun et al., 2010; Spencer et al., 1999; Paranicas et al., 2009), though the analogy with the Mimas thermal anomaly is not straightforward, because at Europa energetic electrons will preferentially impact the trailing side (Paranicas et al., 2001).

4. Conclusions

It has been understood for a long time that radiation affects the chemical properties of ice satellite surfaces (e.g. Johnson, 2004), and alterations of surface physical structure by radiation has also been proposed to explain Ganymede's polar caps (Khurana et al., 2007). However, the results presented here provide the strongest evidence yet that magnetospheric bombardment can change the

physical structure of a planetary surface, and provide strong constraints on the particles responsible, and the nature of the changes. More work is required to determine how the UV reflectance and thermal properties of water ice vary with such bombardment, and how wide-spread such anomalies are throughout the jovian and saturnian systems.

Acknowledgments

The authors would like to thank the Cassini project and especially the CIRS team that made these data possible. They would also like to thank Elias Roussos for his work in updating the energy deposition contours and for help interpreting the Cassini/MIMI data at the highest energies. This work was supported by the Cassini project.

References

- Acton, C., 1996. Ancillary data services of NASA's navigation and ancillary information facility. *Planet. Space Sci.* 44, 65–70.
- Baragiola, R., Fama, M., Loeffler, M., Raut, U., Shi, J., 2008. Radiation effects in ice: New results. *Nucl. Instrum. Methods Phys. Res. B* 266, 3057–3062.
- Cooper, J., Cooper, P., Sittler, E., Sturmer, S., Rymer, A., 2009. Old faithful model for radiolytic gas-driven cryovolcanism at Enceladus. *Planet. Space Sci.* 57, 1607–1620.
- Davies, A., 1996. Io's volcanism: Thermo-physical models of silicate lava compared with observations of thermal emission. *Icarus* 124, 45–61.
- Flasar, F.M. et al., 2004. Exploring the Saturn system in the thermal infrared: The Composite Infrared Spectrometer. *Space Sci. Rev.* 115, 169–297.
- Howett, C., Spencer, J., Pearl, J., Segura, M., 2010. Thermal inertia and bolometric Bond albedo values for Mimas, Enceladus, Tethys, Dione, Rhea and Iapetus as derived from Cassini/CIRS measurements. *Icarus* 206, 573–593.
- Ingemarsson, P., Hedin, A., Sundqvist, B., Tombrello, T., Johnson, R., 1989. Electronic effects in MeV ion tracks affecting thin film adhesion. *Radiat. Effects Defects Solids* 108, 205–209.
- Johnson, R., 2004. *Jupiter: Planet, Satellites and Magnetosphere*. Cambridge University Press, pp. 485–512 (Chapter Radiation Effects on the Surfaces of the Galilean Satellites).
- Jun, I., Garrett, H., Swimm, R., Evans, R., Clough, G., 2005. Statistics of the variations of the high-energy electron population between 7 and 28 jovian radii as measured by the Galileo spacecraft. *Icarus* 178, 386–394.
- Khurana, K., Pappalardo, R., Murphy, N., Denk, T., 2007. The origin of Ganymede's polar caps. *Icarus* 19, 193–202.
- Paranicas, C., Carlson, R., Johnson, R., 2001. Electron bombardment of Europa. *Geophys. Res. Lett.* 28, 673–676.
- Paranicas, C., Cooper, J.F., Garrett, H.B., Johnson, R.E., Sturmer, S.J., 2009. *Europa. University of Arizona Press*, pp. 529–544 (Chapter Europa's Radiation Environment and its Effect on the Surface).
- Paranicas, C. et al., 2011. Energetic charged particle weathering of Saturn's inner satellites. *Planet. Space Sci.*, in press.
- Rathbun, J., Rodriguez, N., Spencer, J., 2010. Galileo PPR observations of Europa: Hotspot detection limits and surface thermal properties. *Icarus* 210, 763–769.
- Raut, U., Fama, M., Loeffler, M., Baragiola, R., 2008. Cosmic ray compaction of porous interstellar ices. *Astrophys. J.* 687, 1070–1074.
- Rozitis, B., Green, S., 2011. Directional characteristics of thermal-infrared beaming from atmosphereless planetary surfaces – A new thermophysical model. *Mon. Not. R. Astron. Soc.* 415, 2042–2062.
- Schenk, P., Hamilton, D., Johnson, R., McKinnon, W., Paranicas, C., Schmidt, J., Showalter, M., 2011. Plasma, plumes and rings: Saturn system dynamics as recorded in global color patterns on its midsize icy satellites. *Icarus* 211, 740–757.
- Simonelli, D., Dodd, C., Veverka, J., 2001. Regolith variations on Io: Implications for bolometric albedos. *J. Geophys. Res.* 106, 33241–33252.
- Spencer, J., 1987. *The Surfaces of Europa, Ganymede and Callisto: An Investigation Using Voyager IRIS Thermal Infrared Spectra*. Ph.D. Thesis, University of Arizona.
- Spencer, J., Moore, J., 1992. The influence of thermal inertia on temperatures and frost stability on Triton. *Icarus* 99, 261–272.
- Spencer, J., Lebofsky, M., Sykes, M., 1989. Systematic biases in radiometric diameter determinations. *Icarus* 78, 227–254.
- Spencer, J., Tamppari, L., Martin, T., Travis, L., 1999. Temperatures on Europa from Galileo Photopolarimeter–Radiometer: Nighttime thermal anomalies. *Science* 284, 1514–1516.
- Spencer, J. et al., 2006. Cassini encounters Enceladus: Background and the discovery of a south polar hot spot. *Science* 311, 1401–1405.
- Zombek, M., 1982. *Handbook of Space Astronomy and Astrophysics*. Cambridge University Press, Cambridge, UK.